9-1-2015

Source Mechanism of Small Long-Period Events at Mount St. Helens in July 2005 Using Template Matching, Phase-Weighted Stacking, and Full-Waveform Inversion

Robin S. Matoza
University of California, San Diego

Bernard A. Chouet
U.S. Geological Survey

Phillip B. Dawson
U.S. Geological Survey

Peter M. Shearer
University of California, San Diego

Matthew M. Haney
U.S. Geological Survey

See next page for additional authors

Authors
Robin S. Matoza, Bernard A. Chouet, Phillip B. Dawson, Peter M. Shearer, Matthew M. Haney, Gregory P. Waite, Seth C. Moran, and T. Dylan Mikesell

AGU PUBLICATIONS

JGR

Journal of Geophysical Research: Solid Earth

RESEARCH ARTICLE
10.1002/2015JB012279

Key Points:
- Source mechanism of small long-period (0.5–5 Hz) subevents at Mount St. Helens
- Volumetric source consistent with shallow subhorizontal crack
- Similar tiny long-period subevents likely part of source process at other volcanoes

Supporting Information:
- Figure S1
- Figure S2
- Figure S3
- Figures S1–S3 captions and Table S1

Correspondence to:
R. S. Matoza,
matoza@geol.ucsb.edu

Citation:
Matoza, R. S., B. A. Chouet, P. B. Dawson, P. M. Shearer, M. M. Haney, G. P. Waite, S. C. Moran, and T. D. Mikesell (2015), Source mechanism of small long-period events at Mount St. Helens in July 2005 using template matching, phase-weighted stacking, and full-waveform inversion, *J. Geophys. Res. Solid Earth*, *120*, 6351–6364, doi:10.1002/2015JB012279.

Received 11 JUN 2015
Accepted 11 AUG 2015
Accepted article online 14 AUG 2015
Published online 18 SEP 2015

Source mechanism of small long-period events at Mount St. Helens in July 2005 using template matching, phase-weighted stacking, and full-waveform inversion

Robin S. Matoza[1,2], Bernard A. Chouet[3], Phillip B. Dawson[3], Peter M. Shearer[1], Matthew M. Haney[4], Gregory P. Waite[5], Seth C. Moran[6], and T. Dylan Mikesell[7,8]

[1]Institute of Geophysics and Planetary Physics, Scripps Institution of Oceanography, University of California, San Diego, La Jolla, California, USA, [2]Department of Earth Science and Earth Research Institute, University of California, Santa Barbara, California, USA, [3]U.S. Geological Survey, Volcano Science Center, Menlo Park, California, USA, [4]Alaska Volcano Observatory, U.S. Geological Survey Volcano Science Center, Anchorage, Alaska, USA, [5]Department of Geological and Mining Engineering and Sciences, Michigan Technological University, Houghton, Michigan, USA, [6]Cascades Volcano Observatory, U.S. Geological Survey Volcano Science Center, Vancouver, Washington, USA, [7]Department of Earth, Atmospheric and Planetary Sciences, Massachusetts Institute of Technology, Cambridge, Massachusetts, USA, [8]Department of Geosciences, Boise State University, Boise, Idaho, USA

Abstract Long-period (LP, 0.5-5 Hz) seismicity, observed at volcanoes worldwide, is a recognized signature of unrest and eruption. Cyclic LP "drumbeating" was the characteristic seismicity accompanying the sustained dome-building phase of the 2004–2008 eruption of Mount St. Helens (MSH), WA. However, together with the LP drumbeating was a near-continuous, randomly occurring series of tiny LP seismic events (LP "subevents"), which may hold important additional information on the mechanism of seismogenesis at restless volcanoes. We employ template matching, phase-weighted stacking, and full-waveform inversion to image the source mechanism of one multiplet of these LP subevents at MSH in July 2005. The signal-to-noise ratios of the individual events are too low to produce reliable waveform inversion results, but the events are repetitive and can be stacked. We apply network-based template matching to 8 days of continuous velocity waveform data from 29 June to 7 July 2005 using a master event to detect 822 network triggers. We stack waveforms for 359 high-quality triggers at each station and component, using a combination of linear and phase-weighted stacking to produce clean stacks for use in waveform inversion. The derived source mechanism points to the volumetric oscillation (~10 m^3) of a subhorizontal crack located at shallow depth (~30 m) in an area to the south of Crater Glacier in the southern portion of the breached MSH crater. A possible excitation mechanism is the sudden condensation of metastable steam from a shallow pressurized hydrothermal system as it encounters cool meteoric water in the outer parts of the edifice, perhaps supplied from snow melt.

1. Introduction

Long-period (LP, 0.5–5 Hz) seismicity, observed at volcanoes worldwide, plays a central role in our ability to assess and forecast unrest and eruption [e.g., *Chouet*, 1996a; *McNutt*, 1996; *Kawakatsu and Yamamoto*, 2007; *Kumagai*, 2009; *Neuberg*, 2011; *Nishimura and Iguchi*, 2011; *Zobin*, 2012; *Chouet and Matoza*, 2013]. The term LP seismicity includes individual transient LP events and more continuous volcanic tremor signals. Over the past several decades, numerous competing hypotheses and models have emerged to explain LP seismicity [e.g., *Chouet and Matoza*, 2013, and references therein]. Among these hypotheses, LP events at shallow depth (<2 km) in a volcanic edifice are commonly explained by the impulsive excitation and resonance of fluid-filled cracks resulting from magmatic-hydrothermal interactions [e.g., *Chouet et al.*, 1994; *Chouet*, 1996a; *Kumagai et al.*, 2002b; *Nakano et al.*, 2003; *Nakano and Kumagai*, 2005a; *Waite et al.*, 2008; *Matoza and Chouet*, 2010; *Arciniega-Ceballos et al.*, 2012; *Maeda et al.*, 2013].

The dome-building phase of the 2004–2008 eruption of Mount St. Helens (MSH) produced millions of repetitive seismic events with long-period codas and slowly evolving waveforms [*Moran et al.*, 2008; *Thelen et al.*, 2008]. Many of these events occurred with such precise regularity that they were termed "drumbeats" [*Moran et al.*, 2008], a phenomenon that has been observed at several other volcanoes [e.g., *Neuberg*, 2000;

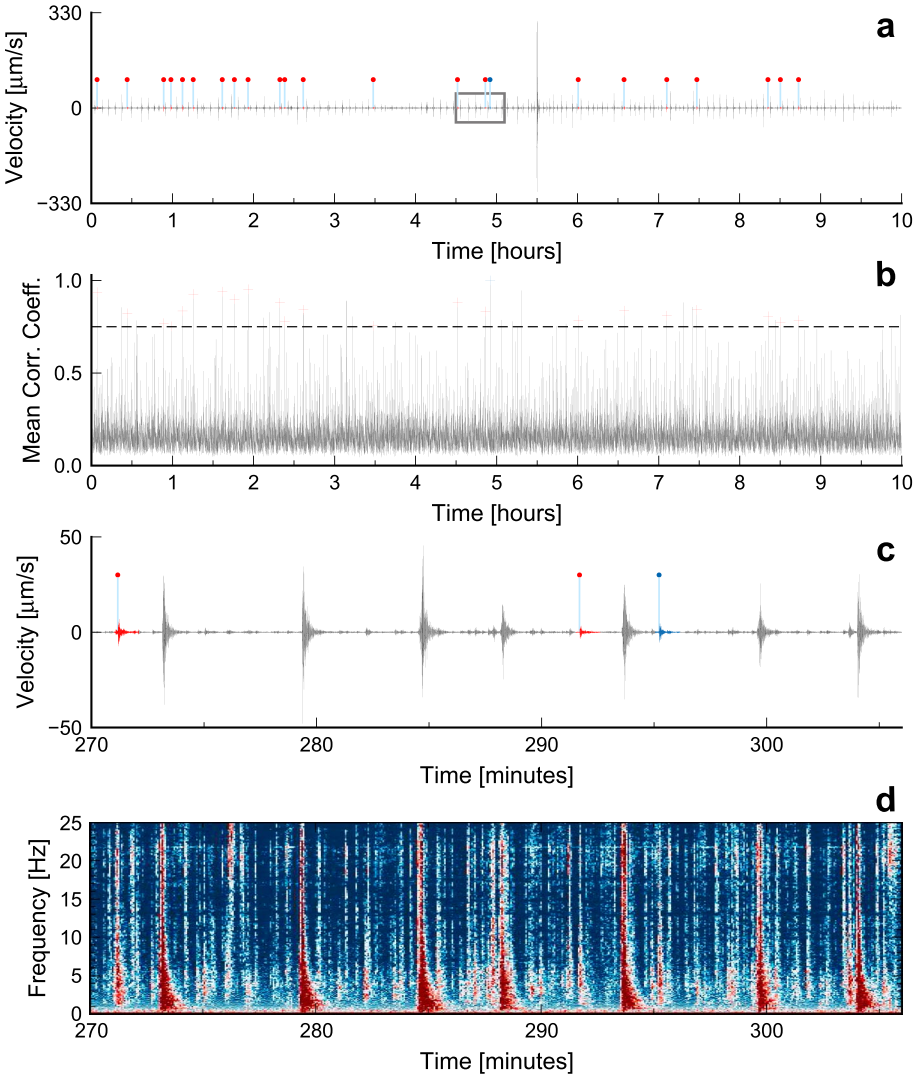

Figure 1. Construction of a master template from 10 h of data from 0800 to 1800 on 2 July 2005. (a) We show the waveform at station S04, vertical component (HHZ) and filtered 0.5–10 Hz, but the template procedure uses all stations and components (see text for details). An initial seed event (blue waveform and vertical pick in Figures 1a and 1c) is used in network-based template matching to detect other similar events (red waveforms and picks in Figures 1a and 1c). The large signal at ~5.5 h is the "large" LP studied by [*Waite et al.*, 2008]. (b) Network-mean correlation coefficient of the seed template with the 10 h data. Horizontal dashed line indicates the detection threshold of 0.75, red crosses are the template matches, and the blue cross is the original seed. Some peaks above the detection threshold are discarded as events due to other criteria (e.g., larger event follows too closely in coda). (c) and (d) show the waveform and spectrogram for a zoomed time window containing the initial seed event (box in Figure 1a).

Lees et al., 2008; *Power and Lalla*, 2010; *Buurman et al.*, 2013; *Firstov and Shakirova*, 2014]. Drumbeat seismicity at MSH has been interpreted in different ways, attributed to shear faulting and brittle failure associated with solid lava spine extrusion and near-surface plug stick-slip [*Iverson et al.*, 2006; *Harrington and Brodsky*, 2007; *Iverson*, 2008; *Kendrick et al.*, 2014] or to the cyclic collapse, resonance, and repressurization of a subhorizontal steam-filled crack within a perched shallow hydrothermal system [*Waite et al.*, 2008; *Matoza et al.*, 2009; *Matoza and Chouet*, 2010]. According to the latter studies, the drumbeat seismic events are volumetric LP events [*Chouet and Matoza*, 2013].

Accompanying the dominant drumbeat LP seismicity throughout the 2004–2008 MSH eruption was a near-continuous, random occurrence of tiny seismic events (Figure 1), recorded most clearly on stations within the breached MSH crater [*Moran et al.*, 2008; *Matoza and Chouet*, 2010]. *Matoza and Chouet* [2010] referred to these events as LP *subevents*, and summarized the temporally evolving properties of their

waveforms, amplitudes, and inter-event recurrence times over several months using largely single-station analysis techniques. Although the subevents often occur within the onset or coda of the larger LP events, they appear to result from a separate random process, only loosely related to cyclic LP drumbeating. Both LPs and subevents were rapidly triggered in response to a phreatic explosion event on 8 March 2005 [*Matoza and Chouet*, 2010]. Here we improve observational constraints on the LP subevents at MSH through full-waveform inversion of precisely aligned network-based stacks of the small, repetitive events.

2. Data

We concentrate on 8 days of continuous velocity waveform data (0000 on 29 June to 0000 on 7 July 2005; all times in UT) from the temporary 19-station three-component Broadband Array at Mount St. Helens (BAMSH) experiment [*Waite et al.*, 2008]. Most stations used Güralp CMG-40T sensors (0.02–30 s); one station (S19) used a Streckeisen STS-2 (0.02–120 s). All stations used Reftek 130 digitizers with a 100 Hz sample rate. This time period was chosen because it contains a large number of small events [*Matoza and Chouet*, 2010] and because it overlaps a particularly large LP event at 1329:50 on 2 July 2005, which was studied in detail by *Waite et al.* [2008]. During our study period, the station availability and network geometry are identical with the study by *Waite et al.* [2008], facilitating comparison with their waveform inversion results for the large LP. In order to optimize this comparison, we follow *Waite et al.* [2008] and use a subset of eight stations (S01, S02, S03, S04, S07, S10, S17, and S19) throughout this paper (for all stages of data processing and inversion), even though other stations contain potentially useful data. We also consider a data duration of 8 days to be a good compromise between stacking a large number of events, and making sure that the waveforms of the individual contributing events are stable and stationary in the time period considered. Previous studies analyzing the temporal evolution of event correlation coefficients at MSH have revealed gradually evolving waveform properties over ~1–2 week time periods [*Thelen et al.*, 2008; *Waite et al.*, 2008; *Matoza et al.*, 2009; *Matoza and Chouet*, 2010; *Hotovec-Ellis et al.*, 2015]. Such waveform changes may result from changes in the seismic velocity structure of the edifice [e.g., as a result of deformation, volumetric strain, and the opening/closing of cracks; *Hotovec-Ellis et al.*, 2015], changes in the topography structure as lava spines were extruded [*Vallance et al.*, 2008], and/or changes in the source. In the fluid-driven crack model [*Waite et al.*, 2008; *Matoza et al.*, 2009; *Matoza and Chouet*, 2010], source waveform changes could arise from changes in the overburden pressure in a hydrothermal system as lava spine mass evolves above, as well as from variations in other magmatic-hydrothermal conditions [*Matoza and Chouet*, 2010].

3. Stacking Small, Repetitive Events

The signal-to-noise ratios (SNR) of the subevents are too low to produce reliable inversion results, but the subevents are repetitive and can be stacked to increase SNR. In this paper, we focus on a single cluster (multiplet) of small subevents, though our methodology could be generalized to consider multiple multiplets. We detect similar small events using a network-based template matching (matched filter) approach [e.g., *Gibbons and Ringal*, 2006; *Shelly et al.*, 2007; *Shelly and Hill*, 2011; *Brown et al.*, 2008], stack the waveforms at each station and component for similar events using phase-weighted stacking [*Schimmel et al.*, 2011; *Thurber et al.*, 2014], then perform full-waveform inversion [e.g., *Ohminato et al.*, 1998; *Kumagai et al.*, 2002a; *Chouet et al.*, 2003; *Lokmer et al.*, 2007; *Dawson et al.*, 2011; *Davi et al.*, 2012; *Maeda et al.*, 2013] using the same model parameterization as *Waite et al.* [2008] (identical topography model, velocity model, station configuration, elementary source time functions, etc.). An advantage of the full-waveform inversion approach is that the waveform data do not need to be picked nor aligned with specification of an assumed origin time. It is sufficient that the data from all the stations begin at a common absolute time because a search over hypocenter and implicitly origin time is included in the inversion (section 4). In our template matching approach, we implicitly assume a common source location for similar events, such that the relative arrival times across the network are consistent for each event. This is the first study of which we are aware to perform full-waveform inversion using phase-weighted stack traces.

To construct a master template, we start with a subset of 10 h of data from 0800 to 1800 on 2 July 2005, a time period which includes the 1329:50 large LP event analyzed by *Waite et al.* [2008] (Figure 1). We then manually select a small subevent as a "seed" starting template, defining a 20 s time window starting at 1255:13 on 2 July 2005 containing the event (Figures 1a, 1c, and 1d). We use this same chosen time window on all stations and components to define a network template. For the template matching, we match the envelopes of

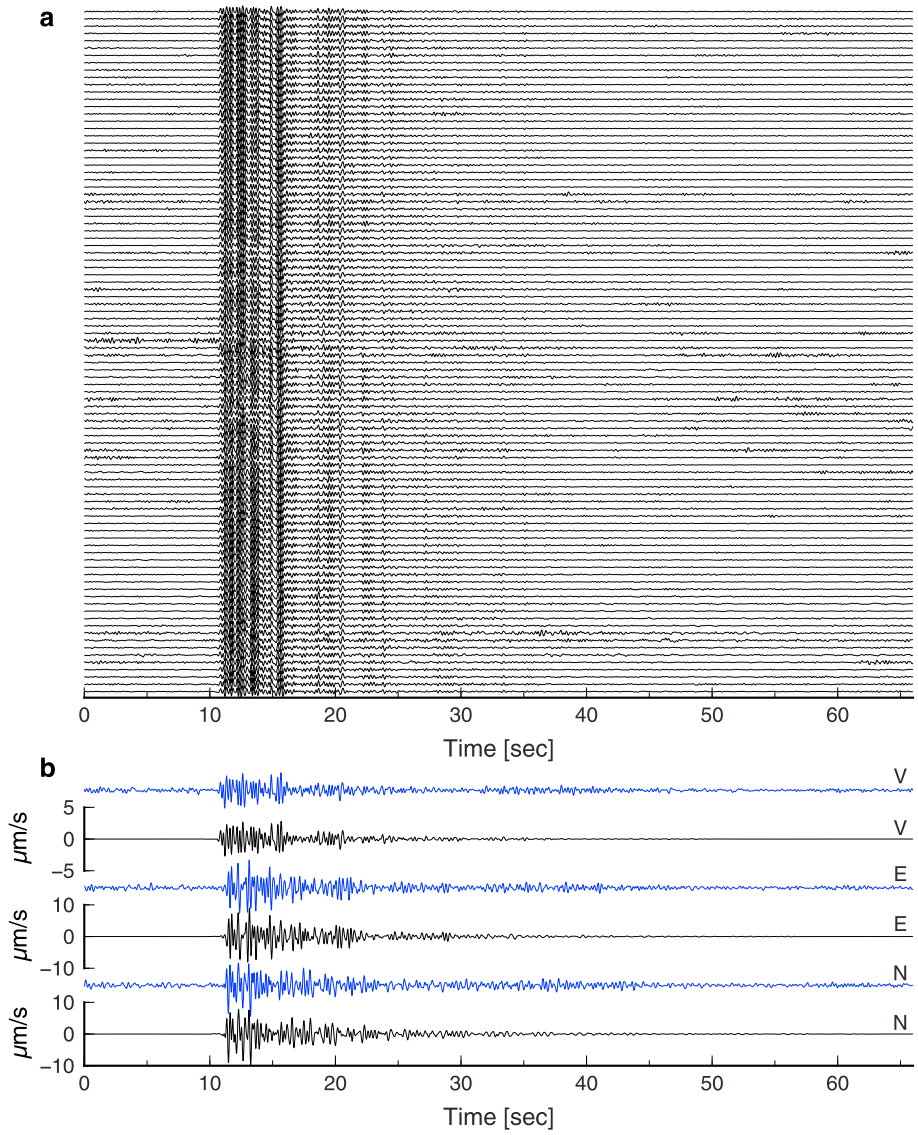

Figure 2. Linear and phase-weighted stacking of waveforms at S04 to produce a final waveform for use in inversion. Each waveform in Figure 2a is a linear stack of all events within a 2 h time period (see text for details) at S04 HHZ (vertical). These 2-hourly linear stacks are then stacked together using phase-weighted stacking to produce the black waveforms in Figure 2b. Figure 2b shows all three components at S04 (V = vertical, E = east, and N = north) for both the final phase-weighted stacks (black) and the initial seed event (blue) (see Figure 1). Note the considerable improvement in SNR from blue to black waveforms. This procedure is performed for all stations and components.

waveform data downsampled to 50 Hz and band pass filtered from 1 to 5 Hz (working with the waveforms rather than the envelopes produces nearly identical results). For each component on every station, we slide the relevant template envelope through the entire 10 h envelope at increments of one sample, computing the absolute value of the correlation coefficient between the template and windows of equal length (20 s) in the 10 h envelope. This results in a time series of correlation coefficients for each station and component. We then linearly stack (average) the correlation coefficient functions across the network to define a network-coincident correlation coefficient function (Figure 1b). We define event triggers as when these averages exceed 0.75 and the events must be more than 20 s apart in time.

We extract the waveforms from 10 s before to 56 s after each trigger (filtered 1 – 5 Hz), and linearly (mean) stack them for each individual station and channel. To avoid the situation where a larger event occurs in the coda of the triggered subevent, we reject from the stack any events where the maximum amplitude is not within 20 s after the trigger on every station and channel. The stacks are performed with normalized waveforms; however,

to preserve physical amplitudes across the network, we rescale the stacks by the original amplitude of the seed event. In total, our master template is constructed from stacking 23 events from the 10 h waveforms (Figure 1a).

We then repeat the procedure (using the same parameters), scanning the master template through the full 8 day waveforms to produce 822 network triggers (using the original seed template instead produces 680 network triggers; thus, the number of events detected is improved using the stacked master template). The triggers are grouped into 2 h time intervals, linear (mean) stacking together all events within each 2 h, now using waveforms reextracted at the trigger times and filtered from 0.5 to 5 Hz (Figure 2a). The waveforms are again windowed from 10 s before to 56 s after the trigger, and we reject from the stack any events where the maximum amplitude is not within 20 s after the trigger. The stacks are performed with normalized waveforms. On average, this procedure stacks about five similar events every 2 h (507 events total).

To produce our final stacks for waveform inversion, we stack the 2-hourly linear stacks (0.5–5 Hz) together using phase-weighted stacking with an exponent of 2 [*Schimmel et al.*, 2011; *Thurber et al.*, 2014]. We choose to perform phase-weighted stacking on 2-hourly linear stacks rather than phase-weighted stacking all individual events (Figure 2). Phase-weighted stacking offers superior SNR gains and cleaner stacks compared to conventional linear stacking; however, it is (1) more computationally intensive and (2) unstable when the individual contributing events are too noisy. Unfortunately, there are occasional drop outs in station/channel availability during the 8 day time period. As a result, we only use 75 2-hourly linear stacks (made up in total of 359 individual events) with the same station and channel availability from an initial 96 2 h periods. We rescale the phase-weighted stacks into physical amplitudes using the initial seed event. Finally, we perform necessary instrumental corrections (e.g., rotating components for misaligned stations) and convert the stacks to the frequency domain for use in waveform inversion. We note that we use waveforms filtered 0.5–2 Hz in the inversion (section 5). However, stacking was performed in the band 0.5–5 Hz, as including the higher frequencies (2–5 Hz) helps produce cleaner stacks (noise stacks more incoherently).

We estimate more complete information about the events during this time period using network-based short-term average/long-term average (STA/LTA) detection. We apply STA/LTA to the eight stations (vertical component) in the band 0.5–10 Hz, with STA length 0.5 s, LTA length 5 s, and an STA/LTA ratio for detection of 1.8. We further require that the STA/LTA triggers are associated across at least four stations within $\pm$1.5 s of a predicted time to each station based on a 1-D velocity model [*Thelen et al.*, 2008] and a reference location defined as the 2 July 2005 large LP event centroid [*Waite et al.*, 2008]. This method detects 7164 total events in the 8 day time period, with 5426 of these events (75%) being classified as subevents based on a simple amplitude cutoff criterion [*Matoza and Chouet*, 2010] (here we use a cutoff amplitude $\leq$ 8 μm/s at station S04, vertical component, to define a subevent). Therefore, the subevent multiplet analyzed in this paper (822 network template triggers from a single initial seed event) corresponds to about 15% of possible subevents during this time period. Thus, this multiplet represents a small subset of all subevents in the time period, and may not be the most dominant or commonly occurring multiplet. Further work, beyond the scope of the present paper, is required to extend our results to other subevent multiplets using separate seed templates.

To check that ordinary LP events are not being included in the stacks based on template matching, we compared the amplitudes of our template-triggered events at station S04 (vertical component) to those of all triggers identified by the network-based STA/LTA detection. We found that occasional larger events (typical amplitude of LPs in this time period) were included in our stacks based on template matching. This is consistent with the results of *Matoza and Chouet* [2010], who found that multiplets of small subevents occasionally include larger amplitude events. To investigate this further, we repeated our entire procedure (including waveform inversion, section 4) using stricter correlation coefficient criteria (network-mean threshold of 0.85) for template detection. We also ran a second test where we rejected any events with amplitudes greater than the initial small seed event. In both cases, we identify fewer similar events, but our waveform stacks and inversion results are barely distinguishable from the results presented here. Thus, we present the results from the more complete event stacks.

4. Waveform Inversion

The methodology for waveform inversion has been described extensively in previous studies [e.g., *Ohminato et al.*, 1998; *Chouet et al.*, 2003, 2005; *Waite et al.*, 2008; *Dawson et al.*, 2011; *Arciniega-Ceballos et al.*, 2012],

Table 1. Inversion Results[a]

Description	N_m	X_n	Y_n	Z_n	X (m)	Y (m)	Z (m)	E_1 (%)	E_2 (%)	AIC(E_1)	AIC(E_2)	γ
Subevent solution 1	9	203	185	269	4060	3700	2120	45.33	107.32	-43733	5829	0.010
Subevent solution 1	6	203	185	269	4060	3700	2120	63.29	136.85	-25128	19214	0.139
Subevent solution 1	3	203	185	269	4060	3700	2120	72.23	139.32	-18117	19657	-
Subevent solution 2	9	200	182	247	4000	3640	1680	45.21	107.78	-43879	6074	0.529
Large LP	9	219	186	263	4380	3720	2000	54.92	88.02	-135762	-27288	0.078

[a]Number of mechanisms $N_m = [9; 6; 3]$ implies [six moments + three forces; six moments; and three forces], respectively. Source centroids X_n, Y_n, Z_n are 20 m grid nodes from an origin at (558271E, 5112042N) UTM Zone 10 and with respect to reference elevation 3260 m below sea level; X, Y are the corresponding meters from the origin, and Z is meters above sea level. γ (equation (6)) is computed for a subset of solutions. E_1, E_2, and AIC are computed from a 10 s portion of the waveform for the subevent and from a 40 s portion of the waveform for the large LP.

so we only briefly summarize it here. We seek a point source solution consisting of a moment tensor and a single-force vector. The representation theorem for this source is written [*Chouet*, 1996b]:

$$u_n(\underline{x}, t) = M_{pq}(t) * G_{np,q}(\underline{x}, t) + F_p(t) * G_{np}(\underline{x}, t), \tag{1}$$

where the summation convention is assumed ($p, q = 1, 2, 3$), u_n is the nth component of displacement at receiver location $\underline{x}$ and time t, $F_p(t)$ is the time history of a single-force applied in the p direction at the source, $M_{pq}(t)$ is the time history of the pqth component of the moment tensor, and $G_{np}(\underline{x}, t)$ is the tensor of elastodynamic Green's functions relating the nth component of displacement at the receiver at $\underline{x}$ to the pth component

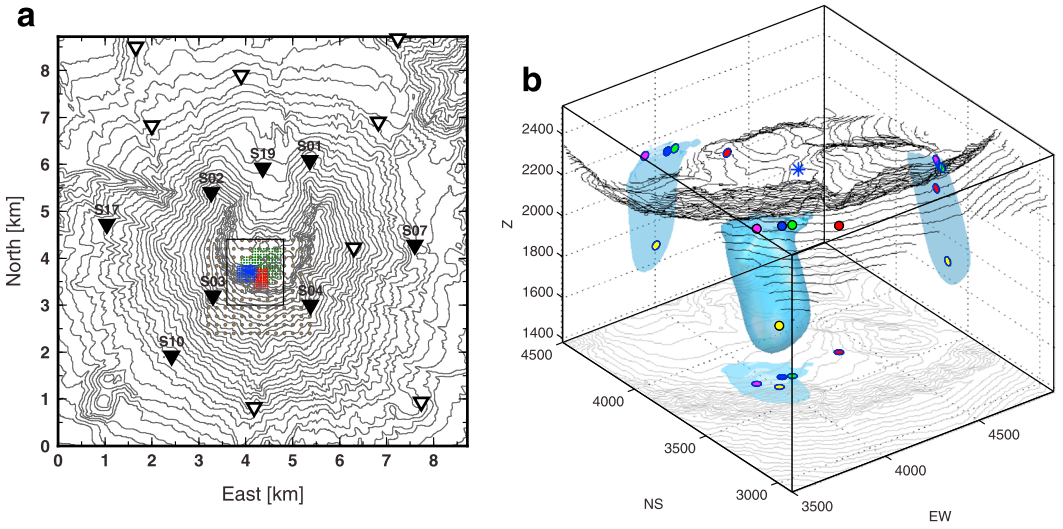

Figure 3. Geometry of the model domain used, shown in kilometers (Figure 3a) and meters (Figure 3b) from an origin at (558271E, 5112042N) UTM Zone 10. The topography model for Mount St. Helens combines a 1980 NAD27 digital elevation model outside the crater, with a model within the crater for topography on 19 April 2005 from aerophotogrammetry [*Schilling et al.*, 2008; *Waite et al.*, 2008]. Contour interval is (Figure 3a) 50 m and (Figure 3b) 20 m. (a) the BAMSH temporary broadband seismic network in this domain is shown by inverted triangles; filled symbols are the eight stations used for waveform inversion. The colored dots represent the surface projections of trial source nodes used in the waveform inversion (orange and green: initial larger, sparser grids; blue: dense grid around best fit solutions for the subevent stack; and red: dense grid for the large 2 July 2005 LP). The box indicates the area of Figure 3b. (b) view from the ~SW showing isosurface of 5% E_1 residual errors above minimum for the subevent stack (light blue surface) with respect to surface topography (contours). Dots indicate source centroids for (blue) the preferred nine-mechanism subevent solution 1; (magenta) minimum E_1 solution; (green) minimum E_2 subevent solution; (yellow) alternative subevent solution 2; and (red) the large LP (see Table 1 and the supporting information). Projections of the isosurfaces and centroids are shown as shadows on the opposite faces of the Cartesian projection. The surface topography is also shown on the lower face for reference. The asterisk marks the surface location of the 4 October 2004 vent; note that the symbol size is smaller than the estimated vent diameter [*Vallance et al.*, 2008]. See also the supporting information Figure S1.

of force applied at the source (the notation ', q' denotes spatial differentiation with respect to q). The frequency domain matrix form of equation (1) is:

$$\mathbf{U}(\omega) = \mathbf{G}(\omega)\mathbf{S}(\omega), \tag{2}$$

where $\mathbf{U}$ is the $N_\tau \times 1$ vector of Fourier-transformed ground displacement components, $\mathbf{G}$ is the $N_\tau \times 9$ matrix of Fourier transforms of synthetic Green's functions, $\mathbf{S}$ is the 9×1 vector of Fourier-transformed force and moment tensor components, and N_τ is the number of observed seismic traces. Equation (2) is of form $\mathbf{d} = \mathbf{Gm}$, which we invert separately for each frequency, recombining the results with inverse Fourier transforms to obtain the desired time domain solutions [*Auger et al.*, 2006]. Note that we perform a "free" inversion, where the mechanism is not constrained to that of a crack or other source geometry [see, e.g., *Nakano and Kumagai*, 2005b]. We invert velocity data then integrate the resulting source time functions to obtain moment and force functions.

We compute the synthetic Green's functions using the three-dimensional (3-D) finite-difference method of *Ohminato and Chouet* [1997], taking into account topography (Figure 3) and a 3-D P velocity (V_p) model [*Waite and Moran*, 2009] and using a 20 m grid spacing, as described by *Waite et al.* [2008]. The 3-D velocity model has a simple structure in the shallow subsurface with heterogeneities on the order of ~1 km. The S wave speed is fixed at $V_p/\sqrt{3}$, and the density is defined with the empirical relation of *Onizawa et al.* [2002]. We use an identical model setup to that of *Waite et al.* [2008] (identical topography model, velocity model, station configuration, elementary source time functions, etc.) to facilitate comparison of our results to those of *Waite et al.* [2008]. Since the point source location is not known a priori, we repeat the inversion at multiple trial source nodes and evaluate the best fit source centroid. To compute Green's functions for multiple trial source nodes, we exploit reciprocity between source and receiver [*Chouet et al.*, 2005]. Figure 3a shows the trial source nodes and the eight three-component stations used for inversion. We gradually refine our calculations, starting with a large and sparse spatial grid of trial source nodes and ending with a denser grid of trial source nodes around the best fit source centroids (Figure 3a).

We evaluate the solutions using the squared error, the relevance of the free parameters, and the temporal stability of the derived source mechanisms. We use two measures of squared error [*Ohminato et al.*, 1998; *Chouet et al.*, 2003]:

$$E_1 = \frac{\sum_{n=1}^{N_\tau}\sum_{p=1}^{N_s}\left(u_n^o(p\Delta t) - u_n^s(p\Delta t)\right)^2}{\sum_{n=1}^{N_\tau}\sum_{p=1}^{N_s}(u_n^o(p\Delta t))^2}, \tag{3}$$

and

$$E_2 = \frac{1}{N_r}\sum_{n=1}^{N_r}\left[\frac{\sum_{j=1}^{3}\sum_{p=1}^{N_s}\left(u_{n,j}^o(p\Delta t) - u_{n,j}^s(p\Delta t)\right)^2}{\sum_{j=1}^{3}\sum_{p=1}^{N_s}\left(u_{n,j}^o(p\Delta t)\right)^2}\right], \tag{4}$$

where $u_n^o(p\Delta t)$ is the pth sample of the nth data trace, $u_n^s(p\Delta t)$ is the pth sample of the nth synthetic trace, N_s is the number of samples in each trace, N_r is the number of three-component receivers, and j represents the three receiver components in equation (4). E_2 weights each station equally because the error is normalized by station, while E_1 is not normalized by station and thus emphasizes the fit on nearby stations that record higher amplitudes. We repeat the inversions for a varying number of assumed mechanisms, $N_m = [9; 6; 3]$, implying [six independent moments + three forces; six moments; and three forces], respectively; where N_m is the number of source mechanism components. We evaluate the significance of the number of free parameters using Akaike's information criteria (AIC) [*Akaike*, 1974]:

$$\mathrm{AIC} = N_\tau N_s \ln E + 2N_m N_f, \tag{5}$$

where N_f is the number of frequencies used in the inversion and E is the residual error, either E_1 or E_2. After identifying a dominantly volumetric source, in a subsequent stage we evaluate the source mechanism

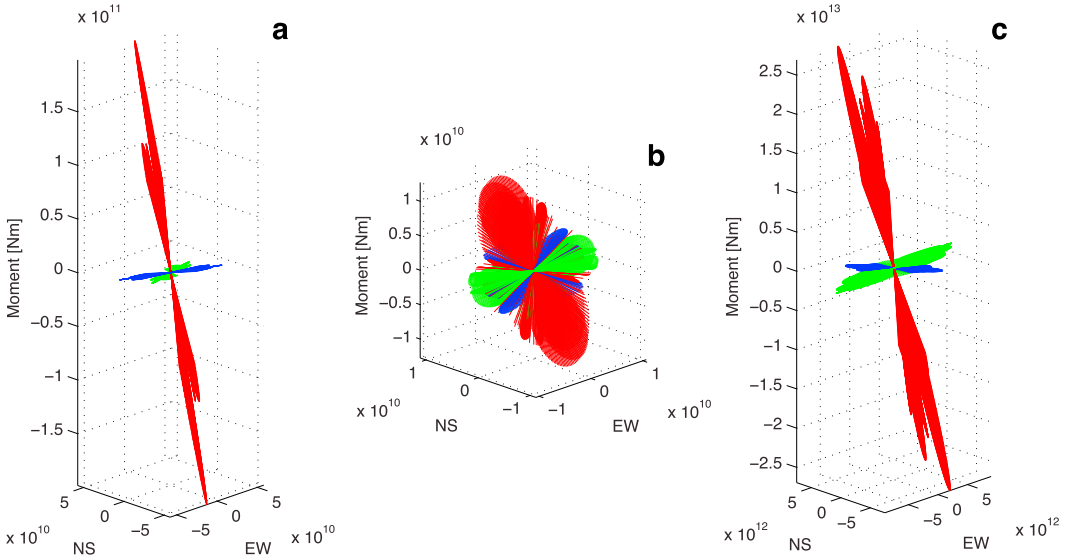

Figure 4. Quiver plots of point-by-point maximum (red), intermediate (blue), and minimum (green) moment tensor eigenvectors scaled by the eigenvalues for (a) the preferred subevent solution 1, (b) the alternative subevent solution 2, and (c) the large LP. Only portions of the source-time functions corresponding to $M_{xx}(t) \geq 0.4 \max\{M_{xx}(t)\}$ are used to construct these plots.

stability by performing a point-by-point eigenvector decomposition of the moment tensor source time functions (Figure 4) and evaluating

$$\gamma = \left[\sigma^2\left(3\frac{\alpha_1}{\alpha_3}\right) + \sigma^2\left(3\frac{\alpha_2}{\alpha_3}\right)\right]^{\frac{1}{2}}, \tag{6}$$

where σ is the standard deviation (over the history of the source time function) and α_1, α_2, and α_3 are the minimum, intermediate, and maximum moment tensor eigenvalues, respectively. Normalization with 3 assumes a Poisson solid with Lamé parameters $\lambda = \mu$. Low values of γ correspond to a temporally stable volumetric moment tensor. We introduce γ as a metric to quantify the stability of a derived volumetric moment tensor.

5. Results

We invert the subevent waveform stack in the band 0.5–2 Hz. For comparison, we also present our replication of the results of *Waite et al.* [2008] for the large LP (inversion performed for 0.25–2 Hz). The 2 Hz upper frequency limit is chosen to be consistent with the work by *Waite et al.* [2008], but we use 0.5 Hz as the low-frequency cutoff because the SNR is low below 0.5 Hz for the subevent stack. All of our solutions are dominated by volumetric components of the moment tensor (Figure 4). The nine-mechanism solutions with moment tensor and single-force components have the lowest AIC values (Table 1) and point to a dominantly volumetric source with a mainly vertical single force.

Given the two definitions of error, we determine that E_1 is better for evaluating the solution for the subevent than E_2 because E_1 gives more weight to nearby stations. We obtain high values of $E_2 > 100\%$ for the subevent (Table 1), where an E_2 of 100% is equivalent to the null solution when $u^s_{n,j} = 0$ in equation (4). The E_2 values greater than 100% indicate that the waveforms at some stations are not well fit by our inversion procedure in the 10 s portion of the waveform selected for calculating errors (see the supporting information Figure S2). We performed additional tests (not shown here), in which we obtained reduced E_2 values (<100%) either by fitting a longer portion of the waveform or by removing some of the more distant stations (S01, S10, and S17) without a change in the derived source mechanism. The high E_2 values likely come from unmodeled velocity structure at distant stations, rather than from low SNR at distant stations; the final waveform stacks have similar SNRs for all stations (see the supporting information for more information on the E_2 error volumes for both the subevent and the large LP).

As shown in Figure 3b and supplementary Figure S1, both the E_1 and E_2 error volumes extend over a depth range within the MSH edifice. However, we find that solutions at greater depth are more unstable. To quantify

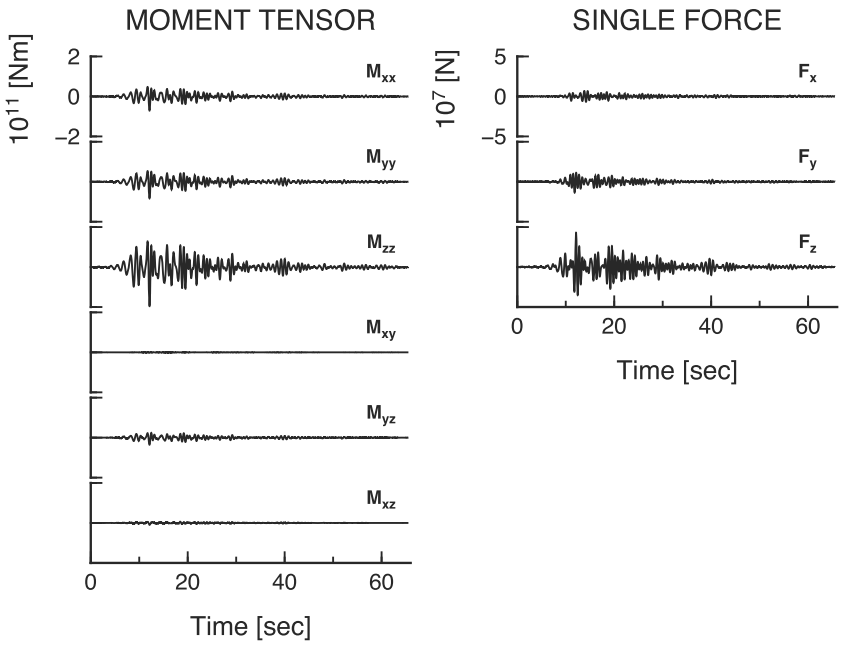

Figure 5. Source time functions for the six independent moment tensor components and three single forces for our preferred subevent source solution at centroid [4060, 3700, 2120] meters. The *y* scales are the same for all moment tensor components and for the single forces. The minimum and maximum amplitudes of each trace are as follows: M_{xx} (-7.1×10^{10}, 4.8×10^{10} N m), M_{yy} (-8.4×10^{10}, 5.3×10^{10} N m), M_{zz} (-2.0×10^{11}, 1.3×10^{11} N m), M_{xy} (-1.5×10^{9}, 1.3×10^{9} N m), M_{yz} (-3.6×10^{10}, 2.4×10^{10} N m), M_{xz} (-8.8×10^{9}, 5.7×10^{9} N m), F_x (-6.8×10^{6}, 6.8×10^{6} N), F_y (-1.4×10^{7}, 1.1×10^{7} N); and F_z (-3.5×10^{7}, 4.3×10^{7} N).

this and choose the most stable solution consistent with the data, we estimate γ (equation (6)) for solutions at all trial source nodes with E_1 within 5% of the minimum and E_2 within 10% of the minimum. We then favor the solution with the smallest γ within these error volumes, resulting in our "preferred" subevent mechanism 1 (Table 1 and Figures 3 and 4). The values of 5% and 10% are chosen so that E_1 has a tighter constraint on the solution than E_2. Our preferred subevent mechanism 1 is within ~120 m of the minimum E_1 solution and within ~45 m of the minimum E_2 solution; it is only 3.6% above minimum E_1 and 2.5% above the minimum E_2.

For illustration, we also present results for an "alternative" subevent mechanism 2 (Table 1 and Figures 3 and 4), corresponding to a local minimum in E_2 at depth (supporting information Figure S1), though this is not near the global E_2 or E_1 minimum. The deeper alternative subevent solution 2 can be modeled as a plexus of cracks, while the shallower preferred mechanism 1 is that of a single subhorizontal crack. Although the derived absolute source location is dependent upon knowledge of the 3-D velocity structure [*Waite and Moran*, 2009], we have analyzed the subevent and large LP event using the same station coverage and model parameterization to permit relative comparison; thus, the subevent is inferred as spatially distinct from the large LP (see the supporting information Figure S1).

The source time functions for the preferred subevent mechanism are shown in Figure 5 (waveform fits are shown in the supporting information Figure S2). The volumetric moment tensor components remain remarkably in-phase through multiple oscillation cycles. The preferred subevent source centroid is ~340 m from (320 m west, 20 m south, and 120 m shallower than) the 2 July large LP event. The preferred subevent source centroid is only 30 m below the topography at this location. A 30 m depth below topography is the shallowest possible source centroid in the staggered-grid scheme of *Ohminato and Chouet* [1997] with our 20 m grid spacing (all moment arms below the free surface). We inspected the Green's functions at this location to ensure that there are no artifacts as a result of proximity to the free surface; the Green's functions vary smoothly with depth from this location. Assuming a Poisson solid with μ = 12 GPa [*Waite et al.*, 2008; *Scheu et al.*, 2006], the volume change [*Chouet*, 1996b] for one peak cycle of the subevent peak to trough is ~10 m^3, roughly 80 times smaller than the 2 July LP. The single-force component is dominantly vertical and peaks at ~0.04 GN, about 200 times smaller than that accompanying the 2 July LP. This force contributes approximately 20% of the observed displacements.

To our knowledge, full-waveform inversion has not previously been applied to phase-weighted stacks. To check that phase-weighted stacking does not introduce artifacts into the derived source mechanism, we perform an additional inversion at the preferred source centroid using data stacks derived from linear stacking only (see the supporting information). In this case, we follow the same workflow but replace the phase-weighted stacking with linear stacking (2-hourly linear stacks are stacked together using linear stacking). The results are similar to those derived here, with a volumetric moment tensor and similar, but slightly noisier, source time functions (supporting information Figure S3).

6. Discussion

There has been debate about the origin of LP or "drumbeat" seismicity associated with the 2004–2008 eruption of MSH [*Chouet and Matoza*, 2013, and references therein]. The link between near–steady state spine extrusion and regular seismicity led to the hypothesis that drumbeats result from shear failure and/or plug stick-slip motion [*Iverson et al.*, 2006, 2008]. *Iverson et al.* [2006] formalized this hypothesis with a mechanical model relating drumbeats to extrusion dynamics of the solid plug forced upward by a constant flux of more molten and compliant magma at depth in the conduit, obtaining a force of $\sim 7 \times 10^7$ N for a slip of 5 mm. In the framework of plug stick-slip, direct estimates of the seismic moment ($M_0 = \mu dA$, where μ is the shear modulus, d is the fault slip, and A is the rupture area) can also be attempted using field observations of the fault surfaces on MSH lava spines [*Pallister et al.*, 2012]. The fracturing on the lava spines is evident at multiple scales, ranging from meter-scale Riedel shears to micron-scale fractures within the fault gouge [*Pallister et al.*, 2012]. Individual megascopic Riedel shear patches seen in outcrops have areas of $\lesssim$100 m^2. Combining this with an inferred slip of ~4 mm, which is based on average plug extrusion rate and seismicity rate and further assumes no aseismic creep [*Pallister et al.*, 2012], the individual Riedel patches are too small to produce the magnitudes of single forces and moments for the 2 July 2005 LP event [*Waite et al.*, 2008] and are also too small to produce the magnitudes of our derived moments and single forces for the stacked subevent. More complex models, such as the simultaneous failure of multiple Riedel structures, are required to explain observed seismic moments [*Pallister et al.*, 2012]. However, the source mechanism derived for the 2 July 2005 LP event by *Waite et al.* [2008] is at odds with a shear faulting and plug stick-slip mechanism.

Our source mechanism and centroid for the subevent are also inconsistent with plug stick-slip. Our preferred subevent mechanism is dominated by volumetric (dipole) moment tensor components with dipole ratios of ~1.00:1.09:3.00, closely approximating 1:1:3 (Figures 4a and 5). This is consistent with volumetric oscillations (opening and closing) of a subhorizontal crack in a Poisson solid ($\lambda = \mu$), which is compatible with a relatively cold hydrothermal environment but inconsistent with hot rock near melting temperatures expected for a magmatic source [*Chouet*, 1996b]. First motions for the subevent stack are emergent and do not provide additional information (supporting information Figure S2). Our preferred subevent centroid has an epicenter ~500 m from the extruding spine (Figure 3b) [see also *Vallance et al.*, 2008] and is located near the base of the south crater wall at the shallowest possible depth in our model (30 m below topography at this location).

The topography data we use for the crater are constructed from aerial photogrammetry on 19 April 2005 [*Schilling et al.*, 2008] and include Crater Glacier [*Walder et al.*, 2008]. Our subevent epicenter is not directly overlain by the glacier, being slightly up the back crater wall; however, the 5% E_1 error volume (Figure 3b) does extend beneath the glacier. Given this location and the small event size, an interesting question is whether the subevents analyzed here might be glacial quakes [e.g., *Weaver and Malone*, 1976; *Walter et al.*, 2009; *West et al.*, 2010; *Thelen et al.*, 2013; *Allstadt and Malone*, 2014]. LP-like events beneath larger-scale glaciers on the flanks of Mount Rainier exhibit mixed first motions, indicating a mechanism of stick-slip basal sliding [*Thelen et al.*, 2013; *Allstadt and Malone*, 2014]. Our volumetric moment tensor is not consistent with stick-slip basal sliding. Our mechanism of a subhorizontal fracture is also inconsistent with basal crevassing, for which we would expect vertically oriented fractures [*Walter et al.*, 2009]. Crevassing is also usually considered an inefficient seismic source poorly coupled to the glacier bed; it is typically only detected at receivers directly on the ice or on rock very close by [*Allstadt and Malone*, 2014]. *Walder et al.* [2008] concluded that Crater Glacier showed no evidence of slip along its bed, indicating that meltwater from Crater Glacier likely did not pond at the glacier bed but instead drained down through the crater bedrock and into the volcano's groundwater system. In general, the glacier was minimally melted by this eruption and did not rapidly produce meltwater [*Walder et al.*, 2008], though *Schilling et al.* [2008] estimate an ice volume loss of ~1.5 ×10^6 m^3 in 1 month from 15 June to 14 July 2005, likely due to glacier melting. If heat were involved in the opening of a bed-parallel fracture at the base of the glacier, we would expect the basal ice to melt rapidly, leading to a short-lived seismic

source inconsistent with our observations. Furthermore, most of the volume loss occurred on the eastern part of Crater Glacier and the western part of the glacier was minimally disturbed through July 2005 [*Walder et al.*, 2008]. East Crater Glacier is topographically lower than the subevent location. Thus, glacier melting was dominantly occurring downhill and well east of the subevent source location and we infer that glacial meltwater did not contribute significantly to the source process for this multiplet.

An alternative explanation is that this subevent multiplet represents an interaction point between a shallow hydrothermal system and cool water in the outer parts of the edifice, possibly supplied by meteoric input such as snow melt. *Matoza and Chouet* [2010] discuss possible scenarios in a pressurized hydrothermal system that could give rise to MSH subevents, based on violent spinodal phase changes or cavitation events [*Thiéry and Mercury*, 2009]. The subevents exhibit waveform stability within multiple distinct multiplets, have Poissonian inter-event times, do not follow a Gutenberg-Richter power law in event size, and were triggered during a phreatic explosion event on 8 March 2005. Based on these event characteristics, *Matoza and Chouet* [2010] hypothesized that MSH subevents represent the randomly occurring but repetitive collapse of voids or cracks at preferential locations within a distributed dendritic hydrothermal crack system [e.g., *Heiken et al.*, 1988]. Our source mechanism and derived volume change of $\sim$10 m^3 for this single-event multiplet is consistent with this picture; by considering only one multiplet, we consider one preferential location within this system. Our source location suggests a possible interaction between a hydrothermal system below and cool water in the volcanic flanks. This scenario is similar to that envisioned by *Maeda et al.* [2013] at Taal Volcano, Philippines, in which the sudden condensation of vapor occurs at a crack tip in a cold aquifer as metastable subcooled gas crosses the gas spinodal [*Thiéry and Mercury*, 2009]. We note, however, that self-potential and time domain electromagnetic imaging of groundwater hydrology has to date been confined to the northern part of MSH crater [*Bedrosian et al.*, 2007, 2008] and neither fumaroles nor anomalous steaming (qualitative indicators of a hot hydrothermal system) have ever been observed near the south crater wall, including during the 2004–2008 eruption. Thus, at this stage, we can only speculate that a shallow pressurized hydrothermal system may be present in the vicinity of the subevent location. The hypocenter is located beneath the south crater wall of MSH, at a location that would have been at a depth of $\sim$500 m prior to the 1980 eruption. Geology in the crater wall at this depth is related to the older MSH volcanic center or andesite and subordinate basalt lava flows, breccia, and scoria of the modern cone [*Voight et al.*, 1981]. We consider that horizontal structure is feasible at this location.

Small LP events similar to MSH subevents have been observed at other volcanoes. For example, within a December 1989 precursory LP swarm at Redoubt, AK, *Stephens and Chouet* [2001] identified low-magnitude "secondary events", and shallow low-amplitude LP multiplets have been imaged at Popocatépetl, Mexico in the band 0.5–2.5 Hz with volume changes of $\sim$1–10 m^3 [*Arciniega-Ceballos et al.*, 2012]. In other instances, the subevents appear as a coupled precursor with a more consistent time delay in relation to the LP event [e.g., *Gil Cruz and Chouet*, 1997; *Caplan-Auerbach and Petersen*, 2005]. We hypothesize that subevents are an integral part of LP seismicity but may often go undetected. The unusual crater geometry of MSH following the 1980 lateral blast [*Voight et al.*, 1981], together with the proximity ($\sim$200 m depth) of the inferred hydrothermal system [*Bedrosian et al.*, 2007, 2008] and LP source [*Waite et al.*, 2008] below the 1980s crater floor, perhaps affords a unique recording geometry. Such tiny seismic events accompanying the main LP source process may not be as easily recorded above noise for LP sources occurring within the depths of a typical uncollapsed stratovolcanic edifice [e.g., *Neuberg et al.*, 2006; *Power and Lalla*, 2010].

7. Conclusions

We applied template matching, phase-weighted stacking, and full-waveform inversion to image the source mechanism of a single multiplet of tiny seismic LP events (subevents) at Mount St. Helens in July 2005. Our source mechanism points to the volumetric oscillation of a subhorizontal crack located at shallow depth ($\sim$30 m) in an area to the south of Crater Glacier at the foot of the south crater wall. We interpret the subevent multiplet as representing an interaction point between a shallow pressurized hydrothermal system and cool meteoric water in the outer parts of the edifice. A possible excitation mechanism involves the violent condensation of steam as metastable subcooled gas crosses the gas spinodal when encountering cool meteoric water. Further work is required to extend our results to other subevent multiplets.

Acknowledgments
We used data from the temporary PASSCAL/USGS BAMSH experiment [*Waite et al.*, 2008], downloaded via IRIS. We used the SAC libraries for processing [*Goldstein and Snoke*, 2005] and GMT for plotting [*Wessel and Smith*, 1991]. This manuscript was improved after careful reviews by two anonymous reviewers and John Lyons. This work was partially supported by NSF awards EAR-1045035, EAR-1446543, and EAR-1113338, and the Cecil H. and Ida M. Green Foundation at the Institute of Geophysics and Planetary Physics, Scripps Institution of Oceanography.

References

Akaike, H. (1974), A new look at the statistical model identification, *IEEE Trans. Autom. Control*, *19*, 716–723, doi:10.1109/TAC.1974.1100705.

Allstadt, K., and S. D. Malone (2014), Swarms of repeating stick-slip icequakes triggered by snow loading at Mount Rainier volcano, *J. Geophys. Res. Earth Surf.*, *119*, 1180–1203, doi:10.1002/2014JF003086.

Arciniega-Ceballos, A., P. Dawson, and B. A. Chouet (2012), Long period seismic source characterization at Popocatépetl volcano, Mexico, *Geophys. Res. Lett.*, *39*, L20307, doi:10.1029/2012GL053494.

Auger, E., L. D'Auria, M. Martini, B. Chouet, and P. Dawson (2006), Real-time monitoring and massive inversion of source parameters of very long period seismic signals: An application to Stromboli Volcano, Italy, *Geophys. Res. Lett.*, *33*, L04301, doi:10.1029/2005GL024703.

Bedrosian, P. A., M. J. Unsworth, and M. J. S. Johnston (2007), Hydrothermal circulation at Mount St. Helens determined by self-potential measurements, *J. Volcanol. Geotherm. Res.*, *160*(1–2), 137–146.

Bedrosian, P. A., M. Burgess, and A. Hotovec (2008), Groundwater hydrology within the crater of Mount St. Helens from geophysical constraints, *Eos Trans. AGU*, *89*(53), Fall Meet. Suppl., Abstract V43E–2191.

Brown, J. R., G. C. Beroza, and D. R. Shelly (2008), An autocorrelation method to detect low frequency earthquakes within tremor, *Geophys. Res. Lett.*, *35*, L16305, doi:10.1029/2008GL034560.

Buurman, H., M. E. West, and G. Thompson (2013), The seismicity of the 2009 Redoubt eruption, *J. Volcanol. Geotherm. Res.*, *259*, 16–30, doi:10.1016/j.jvolgeores.2012.04.024.

Caplan-Auerbach, J., and T. Petersen (2005), Repeating coupled earthquakes at Shishaldin Volcano, Alaska, *J. Volcanol. Geotherm. Res.*, *145*, 151–172.

Chouet, B., P. Dawson, T. Ohminato, M. Martini, G. Saccorotti, F. Giudicepietro, G. D. Luca, G. Milana, and R. Scarpa (2003), Source mechanisms of explosions at Stromboli Volcano, Italy, determined from moment tensor inversions of very-long-period data, *J. Geophys. Res.*, *108*(B1), 2019, doi:10.1029/2002JB001919.

Chouet, B., P. Dawson, and A. Arciniega-Ceballos (2005), Source mechanism of Vulcanian degassing at Popocatépetl volcano, Mexico, determined from waveform inversions of very long period signals, *J. Geophys. Res.*, *110*, B070301, doi:10.1029/2004JB003524.

Chouet, B. A. (1996a), Long-period volcano seismicity: Its source and use in eruption forecasting, *Nature*, *380*, 309–316, doi:10.1038/380309a0.

Chouet, B. A. (1996b), New methods and future trends in seismological volcano monitoring, in *Monitoring and Mitigation of Volcano Hazards*, edited by R. Scarpa and R. I. Tilling, pp. 23–97, Springer, New York.

Chouet, B. A., and R. S. Matoza (2013), A multi-decadal view of seismic methods for detecting precursors of magma movement and eruption, *J. Volcanol. Geotherm. Res.*, *252*, 108–175, doi:10.1016/j.jvolgeores.2012.11.013.

Chouet, B. A., R. A. Page, C. D. Stephens, J. C. Lahr, and J. A. Powers (1994), Precursory swarms of long-period events at Redoubt Volcano (1989–1990), Alaska: Their origin and use as a forecasting tool, *J. Volcanol. Geotherm. Res.*, *62*, 95–135, doi:10.1016/0377-0273(94)90030-2.

Davi, R., G. S. O'Brien, L. De Barros, I. Lokmer, C. J. Bean, P. Lesage, M. M. Mora, and G. J. Soto (2012), Seismic source mechanisms of tremor recorded on Arenal volcano, Costa Rica, retrieved by waveform inversion, *213–214*, 1–13, doi:10.1016/j.jvolgeores.2011.10.008.

Dawson, P. B., B. A. Chouet, and J. Power (2011), Determining the seismic source mechanism and location for an explosive eruption with limited observational data: Augustine Volcano, Alaska, *Geophys. Res. Lett.*, *38*, L03302, doi:10.1029/2010GL045977.

Firstov, P. P., and A. A. Shakirova (2014), Seismicity observed during the precursory process and the actual eruption of Kizimen Volcano, Kamchatka in 2009–2013, *J. Volcanol. Seismolog.*, *8*, 203–217, doi:10.1134/S0742046314040022.

Gibbons, S. J., and F. Ringal (2006), The detection of low magnitude seismic events using array-based waveform correlation, *Geophys. J. Int.*, *165*, 146–166, doi:10.1111/j.1365-246X.2006.02865.x.

Gil Cruz, F., and B. A. Chouet (1997), Long-period events, the most characteristic seismicity accompanying the emplacement and extrusion of a lava dome in Galeras Volcano, Colombia, in 1991, *J. Volcanol. Geotherm. Res.*, *77*, 121–158.

Goldstein, P., and A. Snoke (2005), SAC availability for the IRIS community, Inc. Inst. for Seismol. Data Manage. Cent. Electron. Newsl.

Harrington, R. M., and E. E. Brodsky (2007), Volcanic hybrid earthquakes that are brittle-failure events, *Geophys. Res. Lett.*, *34*, L06308, doi:10.1029/2006GL028714.

Heiken, G., K. Wohletz, and J. Eichelberger (1988), Fracture fillings and intrusive pyroclasts, Inyo Domes, California, *J. Geophys. Res.*, *93*(B5), 4335–4350, doi:10.1029/JB093iB05p04335.

Hotovec-Ellis, A. J., J. E. Vidale, J. Gomberg, W. Thelen, and S. C. Moran (2015), Changes in seismic velocity during the first 14 months of the 2004–2008 eruption of Mount St. Helens, Washington, *J. Geophys. Res. Solid Earth*, *120*, doi:10.1002/2015JB012101, in press.

Iverson, R. M. (2008), Dynamics of seismogenic volcanic extrusion resisted by a solid surface plug, Mount St. Helens, 2004–2005, in *A Volcano Rekindled: The Renewed Eruption of Mount St. Helens, 2004–2006, U.S. Geol. Surv. Prof. Pap. 1750*, edited by D. R. Sherrod, W. E. Scott, and P. H. Stauffer, chap. 6, pp. 425–460, U.S. Geol. Surv., Reston, Va.

Iverson, R. M., et al. (2006), Dynamics of seismogenic volcanic extrusion at Mount St. Helens in 2004–05, *Nature*, *444*, 439–443, doi:10.1038/nature05322.

Kawakatsu, H., and M. Yamamoto (2007), Volcano seismology, in *Treatise on Geophysics. Earthquake Seismology*, vol. 4, edited by H. Kanamori and G. Schubert, pp. 389–420, Elsevier, New York.

Kendrick, J. E., Y. Lavallée, T. Hirose, G. Di Toro, A. J. Hornby, S. De Angelis, and D. B. Dingwell (2014), Volcanic drumbeat seismicity caused by stick-slip motion and magmatic frictional melting, *Nat. Geosci.*, *7*, 438–442, doi:10.1038/NGEO2146.

Kumagai, H. (2009), Source quantification of volcano seismic signals, in *Encyclopedia of Complexity and Systems Science*, edited by R. A. Meyers, pp. 9899–9932, Springer, New York.

Kumagai, H., B. A. Chouet, and M. Nakano (2002a), Waveform inversion of oscillatory signatures in long-period events beneath volcanoes, *J. Geophys. Res.*, *107*(B11), 2301, doi:10.1029/2001JB001704.

Kumagai, H., M. Nakano, and B. A. Chouet (2002b), Temporal evolution of a hydrothermal system in Kusatsu-Shirane Volcano, Japan, inferred from the complex frequencies of long-period events, *J. Geophys. Res.*, *107*(B10), 2236, doi:10.1029/2001JB000653.

Lees, J. M., J. B. Johnson, M. Ruiz, L. Troncoso, and M. Welsh (2008), Reventador Volcano 2005: Eruptive activity inferred from seismo-acoustic observation, *J. Volcanol. Geotherm. Res.*, *176*, 179–190, doi:10.1016/j.jvolgeores.2007.10.006.

Lokmer, I., C. J. Bean, G. Saccorotti, and D. Patanè (2007), Moment-tensor inversion of LP events recorded on Etna in 2004 using constraints obtained from wave simulation tests, *Geophys. Res. Lett.*, *34*, L22316, doi:10.1029/2007GL031902.

Maeda, Y., H. Kumagai, R. Lacson Jr., M. S. Figueroa II, and T. Yamashina (2013), Source process of long-period seismic events at Taal Volcano, Philippines: Vapor transportation and condensation in a shallow hydrothermal fissure, *J. Geophys. Res. Solid Earth*, *118*, 2832–2846, doi:10.1002/jgrb.50205.

Matoza, R. S., and B. A. Chouet (2010), Subevents of long-period seismicity: Implications for hydrothermal dynamics during the 2004–2008 eruption of Mount St. Helens, *J. Geophys. Res.*, *115*, B12206, doi:10.1029/2010JB007839.

Matoza, R. S., M. A. Garces, B. A. Chouet, L. D'Auria, M. A. H. Hedlin, C. De Groot-Hedlin, and G. P. Waite (2009), The source of infrasound associated with long-period events at Mount St. Helens, *J. Geophys. Res.*, *114*, B04305, doi:10.1029/2008JB006128.

McNutt, S. R. (1996), Seismic monitoring and eruption forecasting of volcanoes: A review of the state-of-the-art and case histories, in *Monitoring and Mitigation of Volcano Hazards*, edited by R. Scarpa and R. I. Tilling, pp. 99–146, Springer, Berlin.

Moran, S. C., P. J. McChesney, and A. B. Lockhart (2008), Seismicity and infrasound associated with explosions at Mount St. Helens, 2004–2005, in *A Volcano Rekindled: The Renewed Eruption of Mount St. Helens, 2004–2006, U.S. Geol. Surv. Prof. Pap. 1750*, edited by D. R. Sherrod, W. E. Scott, and P. H. Stauffer, chap. 6, pp. 111–127, U.S. Geol. Surv., Reston, Va.

Nakano, M., and H. Kumagai (2005a), Response of a hydrothermal system to magmatic heat inferred from temporal variations in the complex frequencies of long-period events at Kusatsu-Shirane Volcano, Japan, *J. Volcanol. Geotherm. Res.*, *147*, 233–244, doi:10.1016/j.jvolgeores.2005.04.003.

Nakano, M., and H. Kumagai (2005b), Waveform inversion of volcano-seismic signals assuming possible source geometries, *Geophys. Res. Lett.*, *32*, L12302, doi:10.1029/2005GL022666.

Nakano, M., H. Kumagai, and B. A. Chouet (2003), Source mechanism of long-period events at Kusatsu-Shirane Volcano, Japan, inferred from waveform inversion of the effective excitation functions, *J. Volcanol. Geotherm. Res.*, *122*, 149–164, doi:10.1016/S0377-0273(02)00499-7.

Neuberg, J. (2000), Characteristics and causes of shallow seismicity in andesite volcanoes, *Philos. Trans. R. Soc. A*, *358*, 1533–1546, doi:10.1098/rsta.2000.0602.

Neuberg, J. W. (2011), *Earthquakes, Volcanogenic*.

Neuberg, J. W., H. Tuffen, L. Collier, D. Green, T. Powell, and D. Dingwell (2006), The trigger mechanism of low-frequency earthquakes on Montserrat, *J. Volcanol. Geotherm. Res.*, *153*, 37–50, doi:10.1016/j.jvolgeores.2005.08.008.

Nishimura, T., and M. Iguchi (2011), *Volcanic Earthquakes and Tremor in Japan*, Kyoto Univ. Press, Kyoto.

Ohminato, T., and B. A. Chouet (1997), A free-surface boundary condition for including 3D topography in the finite-difference method, *Bull. Seismol. Soc. Am.*, *87*, 494–515.

Ohminato, T., B. A. Chouet, P. B. Dawson, and S. Kedar (1998), Waveform inversion of very-long-period impulsive signals associated with magmatic injection beneath Kilauea volcano, Hawaii, *J. Geophys. Res.*, *103*, 23,839–23,862, doi:10.1029/98JB01122.

Onizawa, S., H. Mikada, H. Watanabe, and S. Sakashita (2002), A method for simultaneous velocity and density inversion and its application to exploration of subsurface structure beneath Izu-Oshima volcano, Japan, *Earth Planets Space*, *54*, 803–817.

Pallister, J. S., K. V. Cashman, J. T. Hagstrum, N. M. Beeler, S. C. Moran, and R. P. Denlinger (2012), Faulting within the Mount St. Helens conduit and implications for volcanic earthquakes, *Geol. Soc. Am. Bull.*, *125*(3–4), doi:10.1130/B30716.1.

Power, J. A., and D. J. Lalla (2010), Seismic observations of Augustine Volcano, 1970–2007, in *The 2006 Eruption of Augustine Volcano, Alaska, U.S. Geol. Surv. Prof. Pap. 1769*, edited by J. A. Power, M. L. Coombs, and J. T. Freymueller, chap. 1, pp. 3–40, U.S. Geol. Surv., Reston, Va.

Scheu, B., H. Kern, O. Spieler, and D. B. Dingwell (2006), Temperature dependence of elastic P- and S-wave velocities in porous Mt. Unzen dacite, *J. Volcanol. Geotherm. Res.*, *153*, 136–147, doi:10.1016/j.jvolgeores.2005.08.007.

Schilling, S. P., R. A. Thompson, J. A. Messerich, and E. Y. Iwatsubo (2008), Use of digital aerophotogrammetry to determine rates of lava dome growth, Mount St. Helens, 2004–2005, in *A Volcano Rekindled: The First Year of Renewed Eruptions at Mount St. Helens 2004–2006, U.S. Geol. Surv. Prof. Pap. 1750*, edited by D. R. Sherrod, W. E. Scott, and P. H. Stauffer, chap. 8, pp. 145–167, U.S. Geol. Surv., Reston, Va.

Schimmel, M., E. Stutzmann, and J. Gallart (2011), Using instantaneous phase coherence for signal extraction from ambient noise data at a local to a global scale, *Geophys. J. Int.*, *184*, 494–506, doi:10.1111/j.1365-246X.2010.04861.x.

Shelly, D. R., and D. P. Hill (2011), Migrating swarms of brittle-failure earthquakes in the lower crust beneath Mammoth Mountain, California, *Geophys. Res. Lett.*, *38*, L20307, doi:10.1029/2011GL049336.

Shelly, D. R., G. C. Beroza, and S. Ide (2007), Non-volcanic tremor and low-frequency earthquake swarms, *Nature*, *446*, 305–307, doi:10.1038/nature05666.

Stephens, C. D., and B. A. Chouet (2001), Evolution of the December 14, 1989 precursory long-period event swarm at Redoubt Volcano, Alaska, *J. Volcanol. Geotherm. Res.*, *109*, 133–148.

Thelen, W. A., R. S. Crosson, and K. C. Creager (2008), Absolute and relative locations of earthquakes at Mount St. Helens, Washington using continuous data: Implications for magmatic processes, in *A Volcano Rekindled: The First Year of Renewed Eruptions at Mount St. Helens 2004–2006, U.S. Geol. Surv. Prof. Pap. 1750*, edited by D. R. Sherrod, W. E. Scott, and P. H. Stauffer, chap. 4, pp. 71–95, U.S. Geol. Surv., Reston, Va.

Thelen, W. A., K. Allstadt, S. De Angelis, S. D. Malone, S. C. Moran, and J. Vidale (2013), Shallow repeating seismic events under an alpine glacier at Mount Rainier, Washington, USA, *J. Glaciol.*, *59*(214), 345–356, doi:10.3189/2013JoG12J111.

Thiéry, R., and L. Mercury (2009), Explosive properties of water in volcanic and hydrothermal systems, *J. Geophys. Res.*, *114*, B05205, doi:10.1029/2008JB005742.

Thurber, C. H., X. Zeng, A. M. Thomas, and P. Audet (2014), Phase-weighted stacking applied to low-frequency earthquakes, *Bull. Seismol. Soc. Am.*, *104*(5), 2567–2572, doi:10.1785/0120140077.

Vallance, J. W., D. J. Schneider, and S. P. Schilling (2008), Growth of the 2004–2006 lava dome complex at Mount St. Helens, Washington, in *A Volcano Rekindled: The First Year of Renewed Eruptions at Mount St. Helens 2004–2006, U.S. Geol. Surv. Prof. Pap. 1750*, edited by D. R. Sherrod, W. E. Scott, and P. H. Stauffer, Reston, Va.

Voight, B., H. Glicken, R. J. Janda, and P. M. Douglass (1981), Catastrophic rockslide avalanche of May 18, in *The 1980 eruptions of Mount St. Helena, Washington, U.S. Geol. Surv. Prof. Pap. 1250*, edited by P. W. Lipman and D. R. Mullineaux, chap. 6, pp. 347–378, U.S. Geol. Surv., Reston, Va.

Waite, G. P., and S. C. Moran (2009), V_p structure of Mount St. Helens, Washington, USA, imaged with local earthquake tomography, *J. Volcanol. Geotherm. Res.*, *182*, 113–122, doi:10.1016/j.jvolgeores.2009.02.009.

Waite, G. P., B. A. Chouet, and P. B. Dawson (2008), Eruption dynamics at Mount St. Helens imaged from broadband seismic waveforms: Interaction of the shallow magmatic and hydrothermal systems, *J. Geophys. Res.*, *113*, B02305, doi:10.1029/2007JB005259.

Walder, J. S., S. P. Schilling, J. W. Vallance, and R. G. LaHusen (2008), Effects of lava-dome growth on the Crater Glacier of Mount St. Helens, Washington, in *A Volcano Rekindled: The Renewed Eruption of Mount St. Helens, 2004–2006, U.S. Geol. Surv. Prof. Pap. 1750*, edited by D. R. Sherrod, W. E. Scott, and P. H. Stauffer, chap. 13, pp. 257–276, U.S. Geol. Surv., Reston, Va.

Walter, F., J. F. Clinton, N. Deichmann, D. S. Dreger, S. E. Minson, and M. Funk (2009), Moment tensor inversions of icequakes on Gornergletscher, Switzerland, *Bull. Seismol. Soc. Am.*, *99*(2A), 852–870, doi:10.1785/0120080110.

Weaver, C. S., and S. D. Malone (1976), Mt. Saint Helens seismic events: Volcanic earthquakes or glacial noise?, *Geophys. Res. Lett.*, *3*(3), 197–200, doi:10.1029/GL003i003p00197.
Wessel, P., and W. H. F. Smith (1991), Free software helps map and display data, *EOS Trans. AGU*, *72*(41), 441.
West, M. E., C. F. Larsen, M. Truffer, S. O'Neel, and L. LeBlanc (2010), Glacier microseismicity, *Geology*, *38*(4), 319–322, doi:10.1130/G30606.1.
Zobin, V. (2012), *Introduction to Volcanic Seismology*, 2nd ed., Elsevier, Amsterdam.